Inverse Problems in Science and Engineering
Publication details, including instructions for authors and subscription information:
http://www.tandfonline.com/loi/gipe20

Adaptive frequency-domain regularization for sparse-data tomography

Martti Kalke [a] & Samuli Siltanen [a]
[a] Department of Mathematics and Statistics , University of Helsinki , Helsinki , Finland
Published online: 15 Nov 2012.

To cite this article: Martti Kalke & Samuli Siltanen (2013) Adaptive frequency-domain regularization for sparse-data tomography, Inverse Problems in Science and Engineering, 21:7, 1099-1124, DOI: 10.1080/17415977.2012.738678

To link to this article: http://dx.doi.org/10.1080/17415977.2012.738678

Inverse Problems in Science and Engineering, 2013
Vol. 21, No. 7, 1099–1124, http://dx.doi.org/10.1080/17415977.2012.738678

Adaptive frequency-domain regularization for sparse-data tomography

Martti Kalke* and Samuli Siltanen

Department of Mathematics and Statistics, University of Helsinki, Helsinki, Finland

(*Received 15 March 2012; final version received 7 October 2012*)

A novel reconstruction technique, called Wiener Filtered Reconstruction Technique (WIRT), for sparse-data tomographic imaging is introduced in this article. This six-step method applies a spatially-varying constrained least-squares filter combined with a regularization method based on total variation. The WIRT reconstruction is implemented in the frequency domain, where the information based on measurements and regularization can be treated separately. The algorithm applies regularization selectively in the frequency regions where the frequency component values cannot be defined by the measurements. This leads to computational benefits when compared to conventional iterative reconstruction methods such as algebraic reconstruction technique (ART). Both qualitative and quantitative comparisons against state-of-the-art methods suggest that WIRT is a promising reconstruction algorithm for sparse-data imaging regimes, especially with higher noise levels.

Keywords: tomography; sparse data; X-ray imaging; regularization; reconstruction

1. Introduction

Traditional computerized tomography (CT) is based on recording hundreds of X-ray images around the patient during one scan and reconstructing a 3D representation of the internal structures using filtered back-projection. While the image quality of modern CT scanners is excellent, there are two major drawbacks in the abovementioned kind of imaging. First, accurate mechanical movements are required, forcing the device to be massive and expensive. Consequently, scanners are only available in big central hospitals, which radically limits the treatment workflow. Second, the radiation dose is so high that the use of CT imaging is justified only for seriously ill patients.

In recent years there has been an increasing interest in reducing the radiation dose in CT imaging based on the selection of imaging parameters and protocols [1–4]. However, much more dramatic dose reduction is achievable by not using a CT scanner at all, but instead collecting a small number of projection images from different directions with a low-cost X-ray device and computing a 3D reconstruction from such sparse data. As an additional benefit, the workflow is streamlined since the lower device cost allows 3D imaging at smaller clinics. This approach was pioneered by Webber [5–8].

*Corresponding author. Email: martti.kalke@gmail.com
This version has been corrected. Please see Erratum (http://dx.doi.org/10.1080/17415977.2013.820872).

The clinically most widespread example of sparse-data 3D X-ray imaging is the volumetric tomography (VT) dental tomograph, which is based on limited-angle projection data collected with a panoramic X-ray imaging device [9,10]. According to Ludlow et al. [11], VT has the lowest radiation dose among its dense-data competitors:

Modality	Dose (μSv)
Head CT	2100
CB Mercuray	558
NewTom 3G	59
VT device	13

In the above table we use the fact that the dose of the VT device is between one and two panoramic 2D images, whose dose is known to be roughly 6.7 μSv [12,13].

There is a caveat in sparse-data 3D imaging, though. Since there are only few projection images, the reconstruction problem is very sensitive to measurement noise and other unidealities in the imaging chain. Filtered back-projection does not deliver satisfactory results when applied to sparsely sampled data, so other algorithms are called for. Nevertheless, reconstructions from sparse data cannot usually be expected to be as good as from densely sampled CT data. Thus, the philosophy of sparse-data tomography imaging is the following: keep the radiation dose low by collecting as few data as possible while still enabling a good-enough reconstruction for the clinical purpose at hand.

Let us discuss the sparse-data reconstruction problem. From a mathematical perspective, a finite number of line integrals does not determine the volume uniquely since the measurement operator has a nontrivial nullspace [14, Theorem 4.2]. However, the 'ghosts', or the objects invisible in the tomographic data, are well-understood [15–18]. For dense data they are very high-frequency functions, but for sparse data this is not the case and powerful regularization is needed for suppressing the ghosts.

The idea of regularization is to complement the sparse measurement data with *a priori* information. The amount of *a priori* information needed in 2D sparse-data tomography can be estimated quantitatively as follows. The celebrated Fourier–Slice theorem describes how the measured X-ray data is equivalent to knowing certain frequency components of the unknown attenuation coefficient [19,20]. Figure 1 shows that the fraction of measured frequency components is below 10% from the total number of frequency components with indicated resolutions if the angular difference exceeds 10 degrees in parallel-beam sparse-data imaging situations. Thus, in such cases over 90% of the spectrum is dominated by information provided by regularization.

We present here a new method, called Wiener Filtered Reconstruction Technique (WIRT), based on adaptive nonlinear regularization implemented in the frequency domain. The basic idea of WIRT is to replace the regularization constant K in Equation (2.1) by two computationally independent terms: a spatially-varying function called *confidence map* and a parameter called *regularization parameter*. The first one is defined by the point spread function (PSF) and noise, and latter by regularization.

Overall, The WIRT algorithm consists of six phases:

(1) Re-sample the sinogram,
(2) Generate the confidence map,

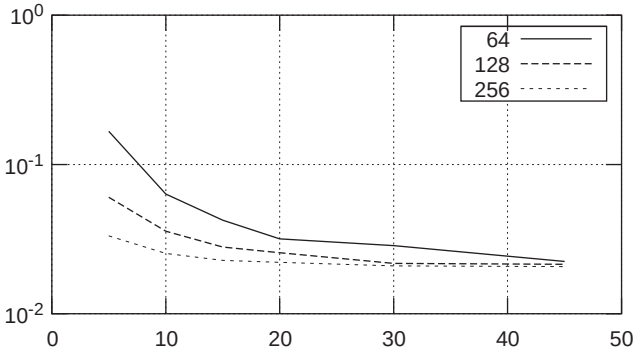

Figure 1. The fraction of known frequency components shown as function of the angular difference in uniformly sampled parallel-beam sparse projection data. We show the fractions at three different resolutions (64×64, 128×128, and 256×256). It is clear from the plot that as the sampling becomes sparser, the number of known Fourier components decreases sharply. The vertical axis has logarithmic scale for clarity.

(3) Make a primary reconstruction,
(4) Define the frequency response,
(5) Apply the degradation filter,
(6) Optimize the regularization parameter.

The details of each step are given in Section 3. As demonstrated in Section 4, WIRT delivers results that outperform those by state-of-the-art iterative reconstruction methods, especially with higher noise levels.

Several different approaches have been suggested in the literature for regularizing sparse-data tomographic problems. These include Tikhonov regularization [10], total variation regularization [21–36], strict piecewise-constant attenuation assumption [37–42], level set methods [43–48], modified algebraic reconstruction [49,50], deformable models [51–55], variational methods [56,57], sparsity-promoting methods [58–64], Bayesian methods [23,65–67] and multiresolution-sparsity methods [68–72] (see also the books [73,74] for discrete tomography approaches). The approach closest to the present one is [75] in the sense that they also use variable regularization in the frequency domain. However, the nonlinear adaptation strategy which we apply is completely different.

Our approach can be seen as an adaptive extension of the classical Wiener filter [76–78], which is nowadays a standard technique in general image processing [79–81]. In tomographic imaging, Wiener filtering typically aims at reducing noise in one of the two ways: either removing noise from the projection images before the reconstruction [82], or removing noise from the reconstructed volume [83,84] (see also [85]). Wiener filter has also been successfully combined with other filters to improve the signal-to-noise relation in the low-dose tomographic imaging [86], and combinations with wavelet transform are promising as well [82,87,88]. We would also like to highlight the paper by Shim [89] clarifying the relation between the singular value decomposition (SVD) and the Wiener filter.

It should be noticed that the abovementioned Wiener filtering methods compensate only the un-idealities of the imaging system, and therefore they do not automatically

provide clinically superior image quality. For best visual results, those filters need to be combined with other image processing operations.

The focus of this article is on affine and sparse-data 2D tomographic imaging. The term *imaging geometry* means the spatial position of the X-ray source, detector and volume corners on each projection image. We use the term *affine imaging geometry*, meaning that all X-rays are parallel and orthogonal to the detector plane and the term *sparse imaging geometry* meaning sparsely distributed projection images with relatively large (10–20 degree) equiangular imaging angles all around the object, unless indicated otherwise. Despite that the object is two-dimensional and projection data is one-dimensional in this study, the term *volume* is used for the target object and *projection image* for the projection data to harmonize terminology with tomographic literature. Also, the terms *voxel* for unit element in the volume and *pixel* for unit element in the projection image are used throughout this article.

Finally, local tomography problems are outside the scope of this study. Therefore, the projection images and the imaging geometry is defined so that all attenuation takes place in the volume.

2. Background

The WIRT method is closely related to classical Wiener filtering, so we give a short introduction to the Wiener filter in Section 2.1. Also, the performance of WIRT will be compared in Section 4 with those of the iterative reconstruction techniques called algebraic reconstruction technique (ART) and simultaneous reconstruction technique (SIRT). We provide an overview of ART and SIRT in Section 2.2.

2.1. *Wiener filter*

The purpose of an *inverse filter* is to compensate for the un-idealities and artefacts generated by the imaging system. The simplest way to implement inverse filtering is to divide the Fourier transform of the degraded image by the frequency response of a linear system. This frequency response can be calculated from the Fourier transform of the point spread function (PSF), which is basically the output of the linear system when the input is a unit impulse. The true degradation function is often unknown and needs to be estimated. Therefore, this kind of filtering operation is called *blind deconvolution* since it employs an estimation of the frequency response, which is commonly based on observations, mathematical models or experimentations. [81, Chapter 5.6]

There are three major flaws in applying inverse filter, as described above. First, since the frequency response is in the denominator, small imperfections have a significant effect on the results and therefore the filter is not stable against noise. Second, even if the frequency response would be perfectly modelled, the inverse filter does not involve a noise model. Third, the inverse filter assumes that the frequency response is defined everywhere in the frequency domain, which is not the case, for example, in the limited-angle or sparse-angle tomography.

A number of improvements have been introduced to improve the stability of the inverse filter. One widely applied improvement is to include a regularization term in

the filter. These regulated filters have a general form of

$$F[\xi_1, \xi_2] = \frac{H^*[\xi_1\ \ \xi_2]}{\left|H[\xi_1, \xi_2]\right|^2 + K}, \tag{2.1}$$

where F is the filter, H is the degradation function and K is the regularization term in the two-dimensional frequency domain. Two most common methods are the *constrained least squares filter* and the *minimum mean square error filter*. The latter is better known as *Wiener filter*, named after Norbert Wiener [81].

In the Wiener filter, the regularization factor K is calculated from the power spectra of the undegraded image and noise. As discussed above, these factors are insufficiently known in ill-posed systems, and therefore a constant value for the regularization parameter K is more feasible estimation than a spatially-varying function $K[\xi_1, \xi_2]$. In ill-posed cases, the choice of K is typically based on estimating the signal-to-noise ratio [81, Chapter 5.8].

In the constrained least-square filter, the regularization term K is defined by the Laplacian operator, i.e. $K[\xi_1, \xi_2] = \gamma P[\xi_1, \xi_2]$, where $P[\xi_1, \xi_2]$ is the Laplacian operator in the frequency domain. The drawback of this method is that the parameter γ has to be iteratively defined by an optimization process or case-by-case basis. The first approach is usually time-consuming, and the second requires human interaction.

2.2. *Algebraic reconstruction techniques*

Most X-ray tomography reconstruction methods are based on the backprojection process, where a projection image is projected back to the volume along the paths of the X-rays. When the same process is repeated for each projection image, a low-frequency estimate of the original volume is generated. There are two different state-of-the-art approaches for the computed tomography reconstruction methods: filtered back-projection (FBP) and ART [90, Chapters 11 and 13].

The FBP is based on the inverse Radon transform and it is the most widely used reconstruction technique in medical CT scanners. However, it has been shown in several studies that the FBP is not suitable for noisy or ill-posed situations like sparse-data imaging. This is because the inverse Radon transform requires a high-pass filter to compensate the blurring effect of the back-projection, which amplifies noise and other un-idealities [19,65].

ART can be considered as a family of reconstructions based on the Kaczmarz iteration method (see [20, Chapter 7], [19] and [90, Chapter 13]). The purpose of the ART is to solve the linear equation defined by tomographic imaging set-up. This is done by defining a volume $\hat{x} \in \mathbb{R}^N$ that minimizes the L^2-norm of the residual between the volume and projection images based on the imaging geometry matrix G, i.e.

$$\hat{x} = \underset{x}{\operatorname{argmin}} \|Gx - m\|_2^2, \tag{2.2}$$

where the vector $m \in \mathbb{R}^M$ consists of all the pixels in the projection images, $x \in \mathbb{R}^N$ is a vector consisting of all the voxels in the volume and $G \in \mathbb{R}^{M \times N}$ is the geometry matrix. This approach is less sensitive to noise and other un-idealities, since the exact solution for the voxel values is not needed. Solving (2.2) will lead to the Moore–Penrose

pseudoinversion

$$x^{\dagger} = (G^T G)^{-1} G^T m. \tag{2.3}$$

In practice, the size of the matrix G is too large for the calculations when real clinical data is used. For example, if 400 projection images with a resolution of 680×680 pixels are used to generate a volume of $512 \times 512 \times 450$ voxels, the size of matrix G is then 118 million columns and 185 million rows. Therefore, instead of building the matrix G, ART utilizes the Kaczmarz routine to iteratively find the volume $\hat{x}$ which minimizes (2.2). The ART iteration step is defined as

$$x^{(k+1)} = x^{(k)} - \lambda \frac{\langle x^{(k)}, g_{k+1} \rangle - m_{k+1}}{\langle g_{k+1}, g_{k+1} \rangle} g_{k+1},$$

where k is the iteration round, g_k is k:th row in the geometry matrix G and λ is the relaxation parameter. It can be shown that this algorithm convergences when $0 < \lambda < 2$ (see [66, Chapter 2.4]).

One form of the ART is the SIRT. In this method, instead of updating the volume $\hat{x}$ after each residual calculation, the current guess is updated after calculating all residuals. Then, the correction is based on the average residual of all measurements

$$x^{(k+1)} = x^{(k)} - \lambda \sum_{i=1}^{h} \frac{\langle x^{(k)}, g_i \rangle - m_i}{\langle g_i, g_i \rangle} g_i.$$

The SIRT method is more stable and generates smoother reconstruction than other ART algorithms. Typically SIRT is used combined with another ART algorithms at the beginning of the iteration process [20, Chapter 7].

Since ART and SIRT are both iterative methods, they are also very time-consuming processes. While the FBP can be considered as a real time operation, the ART calculation with similar data can take few minutes. Nowadays, ART algorithms can be easily parallelized because of the fast development of the graphic processing units (GPUs) and multi-core processors. Therefore, ART is more attractive than FBP in the future because of its capability to handle noisy and ill-posed situations [26].

2.3. *Regularization*

Since ART does not include any regularization, the final solution of the iteration process strongly depends on the noise in the projection images. The absence of the regularization produces artefacts due to the reconstruction [23,65]. Lately, a number of methods have been introduced for improving these stability and uniqueness issues (see references in [66, Chapter 2.3]). The most known popular is the Tikhonov regularization defined by

$$\underset{x}{\operatorname{argmin}}(\|Gx - m\|_2^2 + \alpha \|x\|_2^2). \tag{2.4}$$

Here $\|Gx - m\|$ is the data discrepancy term and $\|x\|$ implements the regularization. The *regularization parameter* $\alpha \in \mathbb{R}_+$ determines a trade-off between emphasizing measurements and *a priori* information. The bigger the regularization parameter we use, the more

we emphasize the regularization and vice versa. Equation (2.4) has the unique solution

$$x^{\dagger} = (G^T G + \alpha I)^{-1} G^T m,$$

where $I \in \mathbb{R}^{N \times N}$ is an identity matrix.

3. The WIRT method

We introduce a novel method, called WIRT, for sparse-data imaging, where images are taken typically under 20 equiangular projection. We applied an adaptive and spatially-varying constrained least-square filter based on the known frequency response of the imaging chain and the estimation of the noise model. In this section, we will introduce the theoretical background of the six phases given in Section 1.

3.1. *Re-sampling the sinogram*

When reconstructing objects from sparse-angle or limited-angle data, we typically get an reconstruction where the resolution depends on the imaging angle. This anisotropic resolution is an undesired situation since it generates artefacts to the final reconstruction, which can be observed as locally blurred edges or distortion of the object (as an example, see the left image in Figure 10).

The purpose of this re-sampling phase is to gain an isotropic reconstruction, which means that the reconstruction should have a resolution independent from the imaging angle. To gain isotropic resolution in the final reconstruction, we balance the number of samples in projection images and the total number of projection images in the sinogram. This phase has two steps: first, new projection images will be generated by using linear interpolation method. Second, projection images will be re-sampled to compensate the truncation error generated in the interpolation process. Since the down-sampling step in this phase blurs the image, we try to avoid too big sampling factor.

Sinogram is a representation of the Radon transform, where horizontal axis is the imaging angle and vertical axis is the distance from the rotation centre. See Figures 8 and 9 for an example of a sinogram. In the sinogram, a single point in the volume makes a trace of

$$f(\theta, \hat{s}) = \hat{s}\cos(\theta), \tag{3.1}$$

where $\hat{s} \leq \frac{N}{2}$ is a distance from the centre of the projection image to the point, N is the number of samples in one projection image and θ is the projection angle. In the sparse equiangular imaging, geometry holds for every $k = 1, 2, 3, \ldots, M$, such that $0 \leq \theta_k \leq \pi$ and $\Delta\theta = \pi/(M-1)$, where M is the number of projection images.

The truncation error $\varepsilon(\theta)$ of the linear interpolation satisfies

$$\left|\epsilon(\theta)\right| = \left|f(\theta, \hat{s}) - P(\theta_1, \theta_2)\right| \leq \frac{(\theta_2 - \theta_1)^2}{8} \max_{\theta_k \leq \xi \leq \theta_{k+1}} f''(\xi), \tag{3.2}$$

where $P(\theta_1, \theta_2)$ is the linear interpolation between the sampling points θ_1 and θ_2 [91, Thorem 5.3.1]. From Equation (3.1) we see that $f''(\xi) = -\hat{s}\cos(\xi)$, which gains its maximum value when $\xi = \pi$ and $\hat{s} = N/2$. The truncation error in the Equation (3.2) can be

reduced to the form of

$$\max\left|\epsilon(\theta)\right| = \frac{(\Delta\theta)^2}{8}\left(\frac{-N}{2}\cos(\pi)\right) = \frac{N(\Delta\theta)^2}{16}. \tag{3.3}$$

Since the truncation error should be less than one pixel, we get an optimal value for the projection image size N_o as

$$N_o = \min\left\{\left\lfloor\frac{16}{(\Delta\theta)^2}\right\rfloor, N\right\}, \tag{3.4}$$

where the operator $\lfloor\cdot\rfloor$ stands for downward rounding. If the down-sampling is needed ($N > 16/(\Delta\theta)^2$), a suitable low-pass filter should be applied prior to the down-sampling process to avoid artefacts in the final reconstruction.

For the sufficient sampling rate, the number of projections should be $M_\tau \approx \frac{\pi N}{2}$ where N is the number of sampling points on each projection image [20, Chapter 5.1.1]. Moreover, for the known interpolation factor a and the number of measured projection images M_0, the total number of projection images is $M_\tau = M_0 + aM_0$. The optimal interpolation factor a in an equiangular case is then

$$a = \left\lceil\frac{N\pi}{2M_0} - 1\right\rceil, \tag{3.5}$$

where $\lceil\cdot\rceil$ is the upward rounding operator. In the interpolation process, the linear interpolation has been applied since it does not produce a piece-wise constant result like the nearest neighbour interpolation and it generates less computational burden than bi-cubic interpolation. Figures 8 and 9 represent the results and errors of the sinogram interpolation.

To simplify the interpolation process, a temporal projection image can be generated by reversing the pixel order in first projection image and defining one extra projection image with an angle of $\pi + \theta_1$ where θ_1 is the angle of first projection image. This can be done based on the fact that in affine imaging geometry $m_k(v, \theta) = m_k(-v, \theta + \pi)$ [20, Chapter 3.2]. After re-sampling, this projection image has to be removed.

For more involved ways to interpolate sinograms, see [92,93].

3.2. *Confidence map*

In this phase, we define a *confidence map* $\Upsilon \in \mathbb{R}^{2N\times 2N}$, where $0 \le \Upsilon_\tau \le 1$ for each complex frequency component τ so that the maximum confidence level indicates the best-known frequency components and zero indicates unknown frequency components based on the projection image geometry.

Since we are estimating uncertainties in extremely ill-posed situation, also the absolute definition of the confidence value is based on approximations and estimations rather than exact knowledge. However, the relative value of the confidence map is more important for reconstruction quality than the absolute value itself, since all confidence map values will be scaled by regularization parameter in the Optimization phase.

For each projection image m_k, the *measured confidence levels* ϑ_k can be defined by the noise of the imaging chain (e.g. behaviour of the X-ray detector and the tube). A practical approach to define the measured confidence levels is to radiate a homogeneous object with fixed radiation X-ray spectra. Since the values of the pixels should be constant,

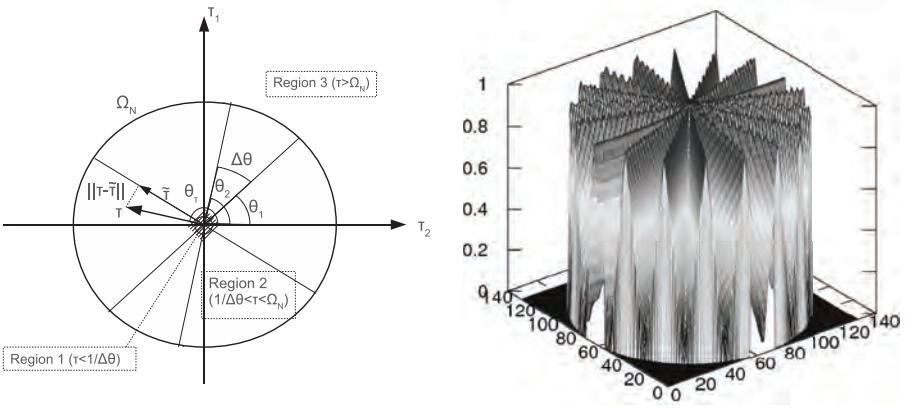

Figure 2. Frequency domain parameters used in the confidence map calculations (left) and example of a confidence map (right).

we can estimate the noise by comparing pixel values m_{ik} to the average value of measurements $\overline{m_k}$ as

$$\vartheta_k = \exp\left(-\frac{\sum_{i=1}^{N}(m_{ik}-\overline{m_k})^2}{N}\right).$$

The exponential function is applied for scaling the confidence map value so that $0 < \vartheta_k \leq 1$ holds. Other models can be utilized depending on the available information about the noise and characteristic behaviour of the imaging chain.

There are three regions in the confidence map (Figure 2). First, the low frequency disc, where the frequency components are well-known, and partly over-sampled, because of the finite quantization. In this area, the confidence value is the maximum of all measured confidence level components. Second, the mid-frequency area, where reliability varies as a function of distance from origin and from the nearest measured confidence level component and therefore the confidence value varies as a function of location. Third, the disc outside the *Nyquist* frequency Ω_N where the confidence level has a value of zero.

The values in an unknown area is based on the distance from the nearest measured confidence level component. This assumption can be justified because when rotating the object the frequency components (specially in low-frequency area) do not change rapidly. Therefore, we can assume that we have better estimation near the measured frequencies and in the low-frequency region than in the high-frequency region far away from the measured frequencies.

Since the confidence value is higher near the known measured frequencies and the origin of frequency domain, the confidence value of Υ_τ, where $1/(\Delta\theta) < \|\tau\| < \Omega_N$, is based on two factors: the distance from the origin and the distance from the nearest measured confidence level component $\tilde{\tau}$. Based on the Fourier slice theorem, the frequency presentation of a single affine backprojection is a line that intersects the origin and has an angle of $\theta + \pi/2$, where θ is the projection angle [20, Chapter 3.2]. The *confidence map* is

therefore defined as

$$\Upsilon_\tau = \begin{cases} \max\{\vartheta_k\} & \text{for } \|\tau\| \leqslant 1/\Delta\theta \\ \Upsilon_{\tilde{\tau}} - \dfrac{\Delta\theta\|\tau\| - 1}{\Delta\theta\Omega_N - 1}\|\tau - \tilde{\tau}\| & \text{for } 1/\Delta\theta < \|\tau\| < \Omega_N \\ 0 & \text{for } \|\tau\| \geqslant \Omega_N, \end{cases} \tag{3.6}$$

where

$$\|\tau - \tilde{\tau}\| = 1 - \left|1 - \frac{2}{\Delta\theta} \mod \left(\left(\theta_\tau - \theta_1 + \frac{\pi}{2}\right), \Delta\theta\right)\right|$$

and θ_τ is the angle of τ comparing to the τ_1-axis, $\Delta\theta$ the angular difference between two projection images and θ_1 is the angle of the first projection image.

3.3. *The primary reconstruction*

The purpose of the *primary reconstruction* is to transform all projection images to the two-dimensional frequency domain by applying the Fourier slice theorem. That theorem relates the one-dimensional frequency domain of a projection with the two-dimensional frequency domain of the volume, and therefore can be considered as a backprojection operator in the frequency domain. This process consists of two phases: the Fourier transform of the projection image and embedding the frequency representations of the projection images into the 2D frequency domain [20, Chapter 3.2].

First, the one-dimensional discrete Fourier transform (1D-DTF) is used to convert the projection images into the frequency domain

$$\widehat{m}_k[\xi, \theta_k] = \sum_{v=1}^{N} m_k[v, \theta_k](-1)^{v-1} \exp(-2i\pi v\xi/N), \tag{3.7}$$

where $m_k[v, \theta_k]$ is a projection image having projection angle of θ_k. Similarly $\widehat{m}_k[\xi, \theta_k] \in \mathbb{C}^N$ is the Fourier representation of the projection image, where ξ is the discrete frequency defined inside the *Nyquist* limits ($-N/2 \leq \xi \leq N/2$). The term $(-1)^{v-1}$ shifts the zero frequency component to the middle of the vector [81, Chapter 4.6.3].

Second, a two-dimensional frequency domain $\omega \in \mathbb{C}^{2N_1 \times 2N_2}$ is created and all frequency components are set to zero as default. Here $N_{1,2}$ are the number of samples in the horizontal and vertical direction and they can be set as $N_{1,2} = N$ (double size comparing to $\widehat{m}_k[\xi, \theta_k]$ is needed for zero padding [81, Chapter 4.7.2]). The element $\omega[N_1, N_2]$ is the zero frequency component and will be considered as the origin of the domain and the axis will be defined as ξ_1 and ξ_2.

Finally, all the frequency representations defined in Equation (3.7) are summed into a two-dimensional frequency domain ω. Since the Fourier transform of the projection image defines the values of the target object along a line subtending the angle θ_k with the ξ_1-axis, summing operation can be specified as

$$\omega[\xi_1, \xi_2] = \sum_{k=1}^{M} \widehat{m}_k[\xi, \theta_k]\delta[c_k], \tag{3.8}$$

where $\delta[c_k]$ is a discrete unit impulse function defined as

$$\delta[c_k] = \begin{cases} 1 & \text{for } c_k = 0 \\ 0 & \text{otherwise.} \end{cases} \tag{3.9}$$

In this case, a value of c_k is set to zero inside the line, that has a projection angle θ_k and intersects the point $[N_1, N_2]$ when $\xi = 0$. That is,

$$c_k = (\xi_1 - N_1)\cos\theta_k + (\xi_2 - N_2)\sin\theta_k - \xi. \tag{3.10}$$

The $\omega[\xi_1, \xi_2]$ in Equation (3.8) is called the primary reconstruction, which is a two-dimensional representation of the volume in the frequency domain based on all backprojected (interpolated or measured) projection images. Since the shifting processes were included in Equations (3.7) and (3.8), the frequency components in the primary reconstruction corresponds to the confidence map.

3.4. *The frequency response of the system*

The frequency response $\zeta[\xi_1, \xi_2]$ describes the behaviour of a linear system in the frequency domain. It can be determined as a Fourier transform of the PSF, also known as an impulse response, which is the output of the system when the input is a unit impulse function (see Equation (3.9)).

Since the projection image is a weighted sum of voxels along a line defined by the projection angle and affine imaging geometry is applied, each projection image can also be considered as a unit impulse function independently from the imaging angle, i.e.

$$m_k[v, \theta_k] = \delta[v - N/2]. \tag{3.11}$$

By merging Equations (3.7), (3.8) and (3.11), we get

$$\zeta[\xi_1, \xi_2] = \sum_{k=1}^{M}\sum_{v=1}^{N} \delta[c_k]\delta[v - N/2](-1)^{v-1} e^{-2i\pi v\tilde{\xi}/N}, \tag{3.12}$$

where $\tilde{\xi} = \xi_1 \cos\theta_k + \xi_2 \sin\theta_k$. Based on fact that Equation (3.12) is non-zero only when $v = N/2$ and $\exp(-i\pi) = -1$, we can simplify that

$$\zeta[\xi_1, \xi_2] = \sum_{k=1}^{M} \delta[c_k](-1)^{N/2-1+\xi_1\cos\theta_k+\xi_2\sin\theta_k}, \tag{3.13}$$

which is the frequency response of the primary reconstruction in the frequency domain. The frequency response consists of M lines which are perpendicular to the imaging angle, intersects the origin and have a constant value of one.

3.5. *Degradation filter*

The purpose of this phase is to define a matrix operator W that reduces the blurring effect generated by the sinogram interpolation and the primary reconstruction processes, and therefore creates an improved reconstruction called *ideal reconstruction*. The relation

between the primary reconstruction Φ and the ideal reconstruction Ψ is then

$$\Psi = W\Phi, \tag{3.14}$$

where $\Phi \in \mathbb{C}^{4N_1N_2}$ as column-wise re-arranged values of the primary reconstruction from Equation (3.8) and therefore defined as

$$\Phi = [\omega(1,1), \omega(2,1), \ldots, \omega(2N_1,1), \omega(1,2), \omega(2,2), \ldots, \omega(2N_1,2N_2)]^T. \tag{3.15}$$

The vector $\Psi \in \mathbb{C}^{4N_1N_2}$ has similar dimensions and component order than Φ.

The matrix $W \in \mathbb{C}^{4N_1N_2 \times 4N_1N_2}$ is determined from three parameters: the confidence map defined by Equation (3.6), the frequency response defined by Equation (3.13), and the regularization.

In well-posed situations we could define the degradation filter based on the inverse of the frequency response since in the affine imaging geometry the PSF is constant and the reconstruction can therefore be considered as a convolution process. Furthermore, convolution is equivalent to element-wise multiplication in the Fourier domain by the Fourier transform of the PSF, which is defined in (3.13).

However, since we have an ill-posed situation and the inverse of the frequency response mentioned above does not exists or at least it is highly unstable, we define the filter W by minimizing the regularized cost function. For that purpose, we introduce two cost functions and bind them together with a regularization parameter.

First, we can simply define the residual between the ideal and primary reconstruction based on the known frequency response, that is

$$F^{(\text{disc})} := \|H\Psi - \Phi\|_2, \tag{3.16}$$

where the frequency response matrix H is defined as

$$H = \lceil \zeta(1,1), \zeta(2,1), \ldots, \zeta(2N_1,1), \zeta(1,2), \zeta(2,2), \ldots, \zeta(2N_1,2N_1) \rfloor, \tag{3.17}$$

where ζ is specified by Equation (3.13).

Second, for regularization purposes, we introduce a spatially-varying Tikhonov regularization in the frequency domain based on the confidence map Υ_τ defined in (3.6). Instead of applying regularization uniformly to all frequency components, we define a diagonal matrix $\Gamma \in \mathbb{R}^{4N_1N_2}$, with diagonal values of $(1 - \Upsilon_\tau)$ corresponding to frequencies in the same way than in matrix H in (3.17). The Tikhonov regularization term then has spatially-varying form of

$$F^{(\text{reg})}(\Psi) := \|\Gamma\Psi\|_2. \tag{3.18}$$

The cost function can be written as the sum of norms (3.16) and (3.18)

$$F(\Psi) := F^{(\text{disc})}(\Psi) + \alpha F^{(\text{reg})}(\Psi),$$

where α is the regularization parameter, which role will be discussed later on. The strategy is to find the minimum point for the F when α is fixed. The ideal reconstruction is then

$$\tilde{\Psi} = \underset{\Psi}{\operatorname{argmin}}(F(\Psi)) = \underset{\Psi}{\operatorname{argmin}}(\|H\Psi - \Phi\|_2^2 + \alpha\|\Gamma\Psi\|_2^2).$$

The gradient of F has a form of

$$\nabla_{\Psi} F(\Psi) = 2H^* H\Psi - H^*\Phi + 2\alpha\Gamma^T\Gamma\Psi,$$

which equals to zero when

$$\Psi = (H^* H + \alpha\Gamma^T\Gamma)^{-1} H^*\Phi. \tag{3.19}$$

Finally, the filter W in Equation (3.14) is defined as

$$W = (H^* H + \alpha\Gamma^T\Gamma)^{-1} H^*. \tag{3.20}$$

As the function F is quadratic, it has a single extreme point, which is the global minimum. Since both matrices H and Γ are diagonal matrices, we can also define Equation (3.19) in element-wise format

$$\psi[\xi_1, \xi_2] = \frac{\overline{\zeta[\xi_1, \xi_2]}}{\left|\zeta[\xi_1, \xi_2]\right|^2 + \alpha(1 - \Upsilon[\xi_1, \xi_2])^2}\,\omega[\xi_1, \xi_2]. \tag{3.21}$$

This can be returned into spatial domain by implementing 2D inverse discrete fourier transform (2D-IDTF), namely,

$$\tilde{x}[k_1, k_2] = \frac{1}{N_1 N_2} \sum_{\xi_1=0}^{N_1-1} \sum_{\xi_2=0}^{N_2-1} \psi[\xi_1, \xi_2] \exp(2i\pi(k_1\xi_1/N_1 + k_2\xi_2/N_2)). \tag{3.22}$$

Finally, the image is moved to the original position and the zero-padded area is removed to gain the final solution for x.

$$x[k_1, k_2] = \left|\tilde{x}\left[k_1 + \frac{N_1}{2}, k_2 + \frac{N_2}{2}\right]\right|, \tag{3.23}$$

where $k_{1,2} = [1, 2, 3, \ldots, N_{1,2}]$. The absolute value operator is needed to eliminate the imaginary part of the x caused by an inaccurate numerical calculation.

3.6. *Optimize the regularization parameter*

Choosing the right regularization parameter α is essential to the final reconstruction quality; if the regularization parameter is too small, artefacts are created by the ill-posed inversion of the frequency response. Moreover, if the regularization parameter is too big, reconstruction will be blurred. See Figure 10 as an example of the regularization effect.

The regularization parameter in the Wiener filter was originally defined by the variance of the additional noise estimation (see, e.g. [81, Chapter 5.7]). However, this approach cannot be applied in the reconstruction model because of the complexity of the imaging chain noise model. For example, the major part of the noise is attached to the detector as a read-out noise and dark current. Moreover, the patient movement, mechanical tolerances and unstable X-ray spectra generates artefacts, which cannot be modelled as a convolution or additional independent Gaussian noise.

Therefore, we introduce a novel approach to define the regularization parameter, which is based on the total variation cost function. The total variation is a suitable model for objects with homogeneous regions and sharp edges, which are expected in the X-ray

tomography reconstructions [23]. The cost functional of the total variation is defined as

$$\Pi(\alpha) = \frac{1}{N_1 N_2} \sum_{k_1=2}^{N_1-1} \sum_{k_2=2}^{N_2-1} \sum_{j_1=-1}^{1} \sum_{j_2=-1}^{1} \left| x_\alpha[k_1 + j_1, k_2 + j_2] - x_\alpha[k_1, k_2] \right|, \tag{3.24}$$

where $x = x_\alpha$ is defined in (3.23) with $0 < \alpha < \infty$ as the regularization parameter, and out-of-bounds summation indices are taken care using periodic boundary conditions.

Since the function (3.21) is monotonic [81, Chapter 5.8], the optimal value for the regularization parameter can be defined by using any robust optimization method. The secant method was chosen for two reasons: the gradient of the cost function is not needed, and both the absolute value and the relative change of the cost function can be calculated with the same computational cost. The secant method is an approximation of the Newton–Raphson method and it has a form of [91, Chapter 4.3]:

$$\alpha^{(h+1)} = \alpha^{(h)} - \Pi(\alpha^{(h)}) \frac{\alpha^{(h)} - \alpha^{(h-1)}}{\Pi(\alpha^{(h)}) - \Pi(\alpha^{(h-1)})}, \tag{3.25}$$

where h is the iteration round.

The algorithm for defining the regularization parameter is the following:

(1) Set the initial value to the regularization parameter $\alpha^{(0)} = 0$.
(2) Execute Equation (3.21) to (3.24).
(3) If the exit criteria (relative or/and absolute) is met, terminate the iteration and consider x as the final reconstruction.
(4) Define a new regularization parameter α based on Equation (3.25).
(5) Go back to step 2.

It should be noticed that the iteration process does not need the forward Fourier transform; the volume is transferred to spatial domain only to calculate the cost function value since the total variation does not have a representation in the frequency domain.

4. Results

We evaluated the reconstruction quality of the WIRT algorithm by comparing it against current state-of-the-art methods, namely ART and SIRT. We coded the ART, SIRT and WIRT algorithms using the Octave program version 3.2.3 with QtOctave interface version 0.8.2 and image processing toolbox on the Ubuntu 10.04 (lucid) distribution environment including Linux version 2.6.32 and GNOME desktop version 2.30.2. The workstation for coding and executing the reconstruction algorithms was a commercially available off-the-shelf desktop PC with 2.40 GHz Dual Core Pentium processor and 8 GB of RAM.

4.1. *Phantoms*

In this study, two different synthetic phantoms (Figure 3) were used. In the first case, we used a standard 128×128 resolution Shepp–Logan phantom, which simulates the inner structures of human head. This phantom is well known in the image processing literature and it was also included in the Octave image processing library. In the second case, we used a CT-slice from the lower jaw, which was originally a region from full dose CT-slice of *dry scull* phantom, meaning a real human jaw inside a plastic-filled head-shaped phantom.

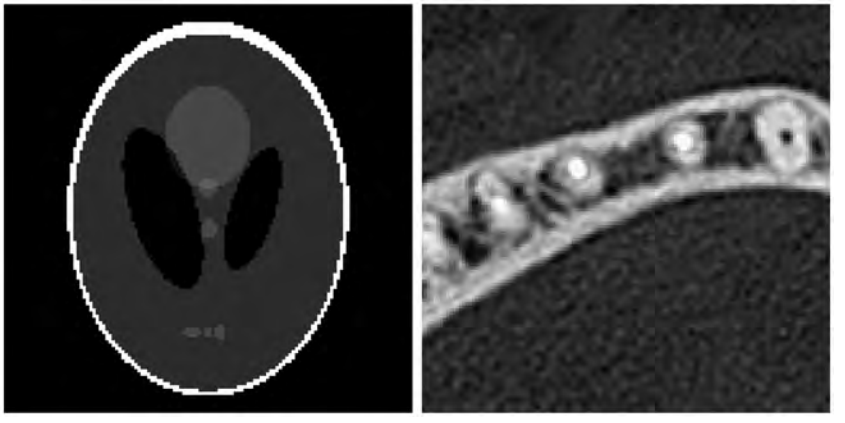

Figure 3. Phantoms used in the evaluation of the reconstructions. Shepp–Logan phantom (left), CT slice from dental arc (right).

This dental arc phantom was chosen to evaluate the reconstruction quality in unisotropic and high-frequency cases, which can be considered as a worst-case scenario for the WIRT algorithm. The size of the volume was 60×60 mm corresponding the voxel size of 0.5 mm. These phantoms were also used as a ground truth in the quantitative image quality analysis.

4.2. *Generation of the projection images*

The projection images were calculated from the phantoms by using an in-built Octave function *Radon*, which calculates the sum of the voxels across the line in the given projection angle. Before the projection calculation, the phantoms were re-sampled by the factor of $\sqrt{2}$ to avoid the inverse crime [66, Chapter 12]. From both phantoms 18 projection images from 43 to 203 degrees with an interval of 10 degrees were calculated. The starting angle was chosen randomly to avoid the over-optimistic reconstruction result caused by direct row-wise or column-wise summation. The size of a single projection image was 185 pixel to guarantee the coverage of whole phantom, which is also in a diagonal direction. In both phantom cases we did two separate studies; noise free and with a 5% Gaussian noise added to all pixels in the projection images.

4.3. *Reconstructions*

For each reconstruction method we set a maximum time of one minute to execute the iteration to guarantee proper comparison. One minute time excluded image geometry-related calculations, like creating geometry matrix G in Equation (2.3) or confidence map Υ in Equation (3.6). However, all calculations which were related to projection image data ware included to the execution time. The relaxation factors for ART and SIRT were 0.9 and 0.11, respectively.

In the WIRT algorithm, there was no need for downsampling because of the demand of a uniform PSF according to Equation (3.4). The interpolation factor was then set to

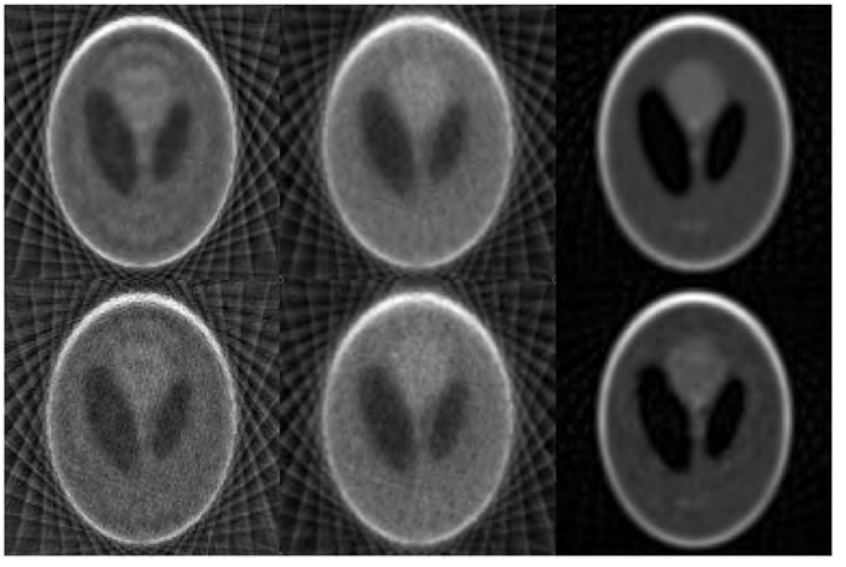

Figure 4. Comparisons of the Shepp–Logan phantom reconstructions. The ART reconstruction (left), the SIRT reconstruction (middle) and the WIRT reconstruction (right). The reconstructions on the upper row are without noise and lower reconstructions has 5% Gaussian noise added to projection images.

11 based on Equation (3.5) ($M_0 = 18$, $N = 185$) and linear interpolation was chosen over cubic and nearest neighbour interpolation to optimize image quality and processing time. In noisy cases, the effect of noise was compensated by reducing the measured confidence level ϑ_k to 0.9 in Equation (3.6). Primary reconstruction was done as explained in Section 3.3 with projection image zero-padding size of 185 pixels.

The PSF was created by creating the unit impulse projection image to the primary reconstruction process instead of directly applying Equation (3.13). The result of the primary reconstruction was then considered as a PSF of this system and implemented in the degradation filter (Equation (3.21)). The exit criteria was set to the magnitude of the total variation under 0.01 defined by Equation (3.24), which was reached in all cases under 10 iterations. The iteration time was 15 seconds in all cases. Results can be seen on the Figures 4 and 5. Furthermore, the profiles from central line are shown in Figures 6 and 7.

4.4. *Error measurement*

The error for the volume residual R_{vol} is defined as root mean square error between the ground truth $\tilde{x}$ and the reconstruction x [81, Chapter 5.8]

$$R_{\text{vol}} = \frac{\|\tilde{x} - x\|}{N_1 N_2} = \frac{1}{N_1 N_2} \sqrt{\sum_{k_1=1}^{N_1} \sum_{k_2=1}^{N_2} (\tilde{x}[k_1, k_2] - x[k_1, k_2])^2}. \tag{4.1}$$

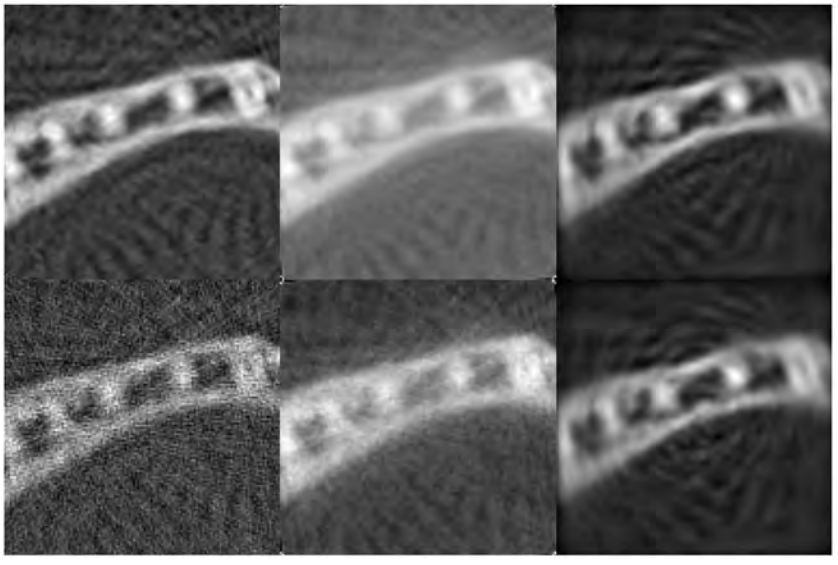

Figure 5. Comparisons of the dental arc reconstructions. The ART reconstruction (left), the SIRT reconstruction (middle) and the WIRT reconstruction (right). The reconstructions on the upper row are without the noise and lower reconstructions has 5% Gaussian noise added to projection images.

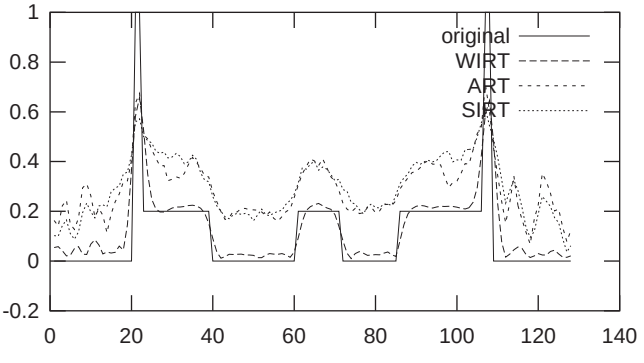

Figure 6. Profiles from 64th row of the Shepp–Logan reconstructions without noise. The profiles are calculated from the upper row images in the Figure 4.

Similarly, the likelihood is defined based on the difference between the original projection images m and the similar projections $\tilde{m}$ calculated from the reconstruction

$$R_{\mathrm{lh}} = \frac{\|\tilde{m} - m\|}{MN} = \frac{1}{MN}\sqrt{\sum_{h=1}^{M}\sum_{k=1}^{N}(\tilde{m}_h[k] - m_h[k])^2}. \tag{4.2}$$

The results in table 1 indicate that WIRT is superior over the ART and SIRT when the reconstruction result is directly compared against the ground truth, which can be seen

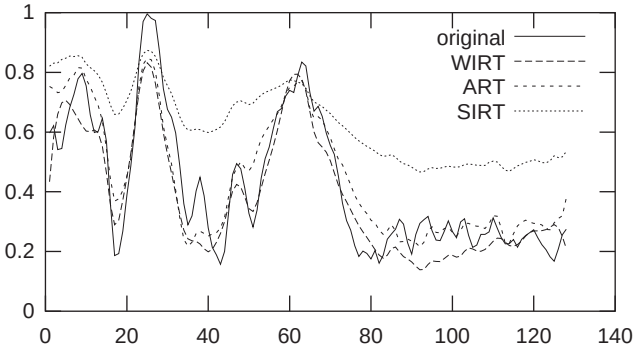

Figure 7. Profiles from 64th row of the dental arc reconstructions without noise. The profiles are calculated from the upper row images in the Figure 5.

Table 1. The root mean square error of the reconstruction described in Equations (4.1) and (4.2) in the Shepp–Logan and dental arc cases with and without noise.

		Noise free			5% Noise		
		ART	SIRT	WIRT	ART	SIRT	WIRT
R_{vol}	Shepp–Logan	917	1416	472	992	1422	494
R_{vol}	Dental arc	426	3056	321	2523	8027	342
R_{lh}	Shepp–Logan	1	57	10	1	57	12
R_{lh}	Dental arc	3	231	5	2	406	9

Note: All values are multiplied by 10^6.

from Figures 4 and 5 as well as in profiles in Figures 6 and 7. The difference is significant specially in the noisy cases. However, when the likelihood errors are compared, the ART reconstruction is slightly better than WIRT. This can be explained by the fact that the principle of ART and SIRT algorithms do not implement any regularization. Therefore, they minimize the likelihood while the WIRT is minimizing both likelihood and regularization terms simultaneously.

5. Discussion

The fundamental difference between WIRT and the reference reconstruction techniques is that WIRT optimizes the image quality based on *a priori* information. This can be seen by comparing the residual values of the volume and likelihood in the Table 1. The data discrepancy is roughly the same in all three methods (ART, SIRT and WIRT), but the residual when comparing the reconstruction volumes itself is superior when using WIRT. The same phenomenon can be seen in the Shepp–Logan profile, especially when comparing SIRT against WIRT.

The reason for better reconstruction in the Shepp–Logan case than in the dental arc case can be explained by dissimilarities in the shape of the phantoms, which can be seen

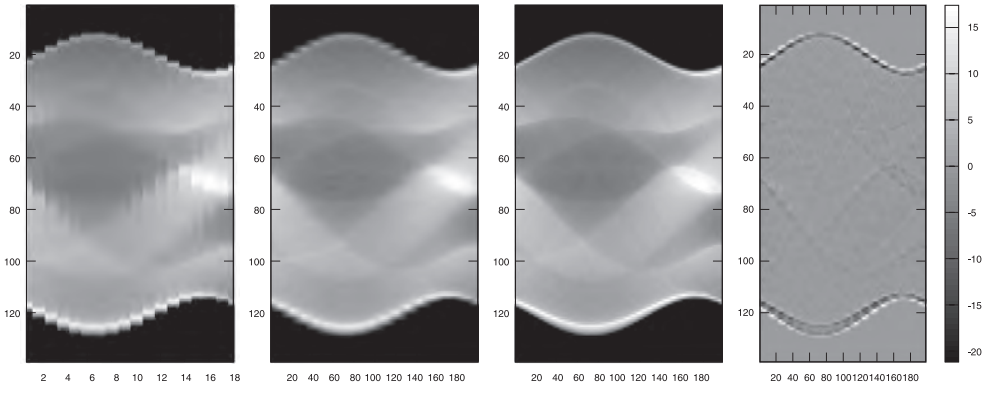

Figure 8. Sinogram of the Shepp–Logan case. Measured sinogram (left), interpolated and full measured sinogram (middle), and the difference between interpolated and full sinogram (right).

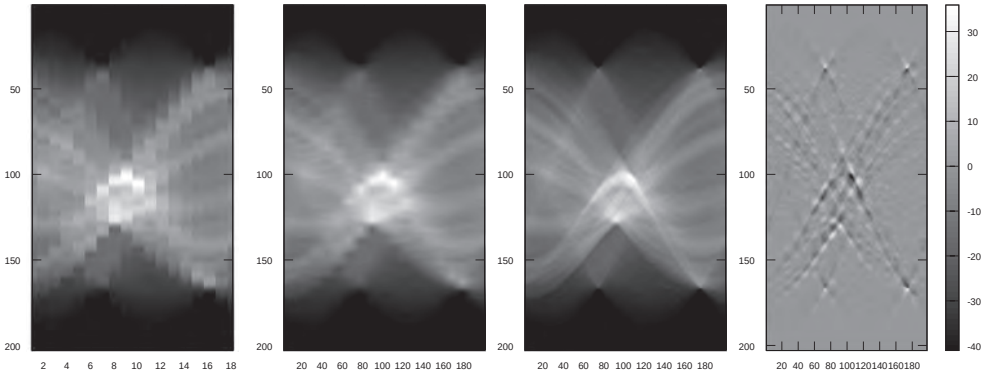

Figure 9. Sinogram of the dental arc case. Measured sinogram (left), interpolated and full measured sinogram (middle), and the difference between interpolated and full sinogram (right).

from the right-hand side of Figures 8 and 9. In the Shepp–Logan case, the magnitude of the difference is half the dental arc case and the differences are located in the peripheral region because of the smooth and round shape of the phantom. In contrast to the Shepp–Logan phantom, the dental arc includes more sharp edges, parts of which are located in the middle of the image. Since the sharp edges generate high-frequency components and the truncation error is higher in high-frequency regions (as described in Section 3.2), the subjective image quality of the dental arc reconstruction is worse than Shepp–Logan phantom (Figure 10).

Using sparse-data imaging, instead of the full-scan CT imaging, decreases the patient dose in several ways. The number of projection images can be significantly decreased without scarifying the clinically needed image quality. Also, since the advanced reconstruction methods are less sensitive to noise, tube current and exposure times, the overall patient dose per projection image can also be decreased.

Lower patient dose can justify 3D imaging in the cases where it has not yet been applied; for example in dental imaging, where some treatments are focusing on the

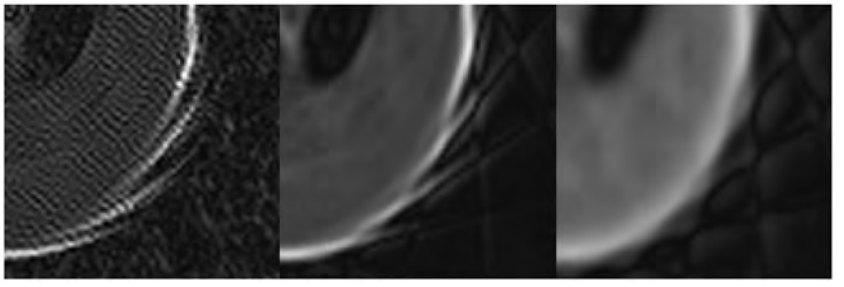

Figure 10. A detail from Shepp–Logan reconstruction and the effect of the regularization. Regularization parameters are from left to right 0, 50 and 2000. Unlike in other cases, the angular difference is 20 degree to emphasize the phenomenon.

cosmetic improvements instead of diagnosing diseases or abnormalities. Furthermore, the sparse-data imaging in X-ray tomography can be used for preview image, where an un-detailed reconstruction is generated to verify the sufficient patient positioning before the final scan or to optimize the imaging related parameters like X-ray voltage, current or number of projection images for the final scan.

Comparing to the statistical inversion methods [23,65–67], the iteration phase in the WIRT has three major benefits. First, since the regularization parameter is a scalar value, the optimization is limited to one dimension, which is computationally more effective. Second, the regularization term in Equation (3.21) vanishes for the known frequency components and therefore there is no need to calculate the likelihood during this iterative operation. Third, the gradient for total variation is irrelevant since the iteration algorithm uses only the absolute value of the cost function.

As it can be seen from Equations (3.21) and (3.24), the operations during the iteration process are element-wise operations. Since these operations have bijective relations, these operations are easier to optimize for parallel calculations in the graphics processing unit or multi-core processor environment. This is not possible in reconstructions in spatial domain, since the relations between voxels and pixels are defined by imaging angles, which relates multiple voxels to the single pixel and vice versa.

Most of the studies on implementing Wiener filters and their variations in tomographic imaging (e.g. [83,84,86–88]) are focusing on image processing either before or after the reconstruction. Moreover, these studies mainly concern the full-scan data, not sparse-angle or limited-angle situations. However, there are also some studies on improving the stability issues in limited-angle cases by implementing the Wiener filter, like articles from Dhawan [94], Jaffe [95] or recently Zdunek et al. [96].

Nevertheless, unlike in our study, none of those do interpret the noise as a uncertainty or optimize the regularization term. Instead of that, Dhawan implements the original limited PSF and models the noise as constant white noise. Jaffe refined this method by defining the Wiener filter from the observed data. Zdunek applied the Wiener filter to improve th Focal Under-determined System Solver (FOCUSS) algorihm and its variations, originally introduced by Gorodnitsky and Rao [97].

The WIRT algorithm described in this study has some limitations, which were introduced to keep the focus on the essential parts of the algorithm routine. First of all, in this article we have concentrated only on equiangular cases and not the random angular or the limited-angle cases. Second, we have concentrated on affine imaging geometry instead

of implementing sinogram modification routines for the fan-beam geometry [20, Chapter 3.5]. Third, we have implemented an optimization process in the spatial domain instead of frequency domain. This slows down the iteration since we have to run IFFT routine on each iteration round to calculate the cost function value.

Generalization of the WIRT by removing the limitations mentioned above can be considered as a future improvement for the WIRT algorithm. Moreover, there are some interesting results using regularization in the wavelet domain by Rantala et al. [68] with interesting benefits, which gives a new viewpoint for implementing the WIRT algorithm in the wavelet space instead of frequency domain.

Wiener filter has been proven to work with other tomographic imaging technologies, like optical coherence tomography (OCT) [98] or electromagnetic geotomography [99]. Despite the fact that we have concentrated only on medical applications, there are other applications like astronomical imaging and tree imaging where WIRT algorithm could nicely fit in.

6. Conclusion

We have proposed a reconstruction method, called WIRT, for sparse-data tomographic imaging situations with a modified constrained least-squares filter. The effectiveness of this algorithm is based on the selective regularization in the frequency domain and implementation of the total variation in the regularization process. We also coded this method in the Octave language and presented the results which indicates that the WIRT algorithm provides a significantly better reconstruction quality than ART or SIRT in the sparse-data imaging scene, specially when noise is present. This can be seen specially in reconstruction images from Figures 4 and 5. Moreover, profiles in Figures 6 and 7 verify that the total variation and the selective regularization preserve the sharp edges better than non-regulated reconstructions.

Acknowledgements

This research project was supported by Instrumentarium Foundation. The authors also thank PaloDEx Group (Tuusula, Finland) and Finnish Inverse Problems Society for support. This work was supported by the Academy of Finland Centres of Excellence in Inverse Problems Research (213476 and 250215) and project 141094.

References

[1] V. Tsapaki, J.E. Aldrich, R. Sharma, M.A. Staniszewska, A. Krisanachinda, M. Rehani, A. Hufton, C. Triantopoulou, P.N. Maniatis, J. Papailiou, and M. Prokop, *Dose reduction in CT while maintaining diagnostic confidence: Diagnostic reference levels at routine head, chest, and abdominal CT—IAEA-coordinated research project*, Radiology 240 (2006), pp. 828–834.

[2] T. Kubo, P.-J.P. Lin, W. Stiller, M. Takahashi, H.-U. Kauczor, Y. Ohno, and H. Hatabu, *Radiation dose reduction in chest CT: A review*, Am. J. Roentgenol. 190 (2008), pp. 335–343.

[3] C.H. McCollough, A.N. Primak, N. Braun, J. Kofler, L. Yu, and J. Christner, *Strategies for reducing radiation dose in CT*, Radiol. Clin. North Am. 47 (2009), pp. 27–40.

[4] L. Yu, X. Liu, S. Leng, J.M. Kofler, J.C. Ramirez-Giraldo, M. Qu, J. Christner, J.G. Fletcher, and C.H. McCollough, *Radiation dose reduction in computed tomography: techniques and future perspective*, Imag. Med. 1 (2009), pp. 65–84.

[5] R. Webber, R. Horton, T. Underhill, J. Ludlow, and D. Tyndall, *Comparison of film, direct digital, and tuned-aperture computed tomography images to identify the location of crestal defects around endosseous titanium implants*, Oral Surg., Oral Med., Oral Pathol., Oral Radiol., and Endodontol. 81 (1996), pp. 480–490.

[6] R.L. Webber, R.A. Horton, D.A. Tyndall, and J.B. Ludlow, *Tuned aperture computed tomography (TACT). theory and application for three-dimensional dento-alveolar imaging*, Dentomaxillof. Radiol. 26 (1997), pp. 53–62.

[7] R.L. Webber and J.K. Messura, *An* in vivo *comparison of diagnostic information obtained from tuned-aperture computed tomography and conventional dental radiographic imaging modalities*, Oral Surg., Oral Med., Oral Pathol., Oral Radiol. and Endodontol. 88 (1999), pp. 239–247.

[8] R.L. Webber, H.R. Underhill, and R.I. Freimanis, *A controlled evaluation of tuned-aperture computed tomography applied to digital spot mammography*, J. Digital Imag. 13 (2000), pp. 90–97.

[9] A. Cederlund, M. Kalke, and U. Welander, *Volumetric tomography — A new tomographic technique for panoramic units*, Dentomaxillofac. Radiol. 38 (2009), pp. 104–111.

[10] N. Hyvonen, M. Kalke, M. Lassas, H. Setala, and S. Siltanen, *Three-dimensional X-ray imaging using hybrid data collected with a digital panoramic device*, Inverse Probl. Imag. 4(2) (2010), pp. 257–271.

[11] J.B. Ludlow, L.E. Davies-Ludlow, S.L. Brooks, and W.B. Howerton, *Dosimetry of 3 CBCT devices for oral and maxillofacial radiology: CB Mercuray, NewTom 3G and i-CAT*, Dentomaxillof. Radiol. 35 (2006), pp. 219–226.

[12] R.A. Danforth and D.E. Clark, *Effective dose from radiation absorbed during a panoramic examination with a new generation machine*, Oral Surg., Oral Med., Oral Pathol., Oral Radiol. Endodontol. 89(2) (2000), pp. 236–243.

[13] S.C. White, *Assessment of radiation risk from dental radiography*, Dentomaxillof. Radiol. 21(3) (1992), pp. 118–26.

[14] K.T. Smith, D.C. Solmon, and S.L. Wagner, *Practical and mathematical aspects of the problem of reconstructing objects from radiographs*, Bull. AMS 83(6) (1977), pp. 1227–1270.

[15] B.F. Logan, *The uncertainty principle in reconstructing functions from projections*, Duke Math. J. 42(4) (1975), pp. 661–706.

[16] Alfred K. Louis, *Orthogonal function series expansions and the null space of the Radon transform*, SIAM J. Math. Anal. 15(3) (1984), pp. 621–633.

[17] Alfred K. Louis, *Nonuniqueness in inverse Radon problems: The frequency distribution of the ghosts*, Math. Z. 185(3) (1984), pp. 429–440.

[18] P. Maass, *The X-ray transform: singular value decomposition and resolution*, Inverse Probl. 3(4) (1987), pp. 729–741.

[19] Frank Natterer, *The Mathematics of Computerized Tomography*, John Wiley and Sons and B G Teubner, Stuttgart, 1986.

[20] A.C. Kak and M. Slaney, *Principles of Computerized Tomography*, SIAM, Philadelphia, PA, 2001.

[21] A.H. Delaney and Y. Bresler, *Globally convergent edge-preserving regularized reconstruction: an application to limited-angle tomography*, IEEE Trans. Image Process. 7 (1998), pp. 204–221.

[22] M. Persson, D. Bone, and H. Elmqvist, *Total variation norm for three-dimensional iterative reconstruction in limited view angle tomography*, Phys. Med. Biol. 46 (2001), pp. 853–866.

[23] V. Kolehmainen, S. Siltanen, S. Järvenpää, J.P. Kaipio, P. Koistinen, M. Lassas, J. Pirttilä, and E. Somersalo, *Statistical inversion for medical X-ray tomography with few radiographs: II. Application to dental radiology*, Phys. Med. Biol. 48 (2003), pp. 1465–1490.

[24] H.Y. Liao and G. Sapiro. Sparse representations for limited data tomography. *Biomedical Imaging: From Nano to Macro, 2008. ISBI 2008. 5th IEEE International Symposium on*, May 2008, pp.1375–1378.

[25] E.Y. Sidky, C.M. Kao, and X. Pan. Effect of the data constraint on few-view, fan-beam CT image reconstruction by TV minimization. In *Nuclear Science Symposium Conference Record, 2006*. IEEE, vol. 4, IEEE, 2006, pp. 2296–2298.

[26] V. Kolehmainen, S. Vanne, S. Siltanen, S. Järvenpää, J.P. Kaipio, M. Lassas and M. Kalke. Parallelized Bayesian inversion for three-dimensional dental X-ray imaging *IEEE Trans. Med. Imaging* 25 (2006), pp. 218–228,

[27] E. Y. Sidky, C.-M. Kao, and P. Xiaochuan, *Accurate image reconstruction from few-views and limited-angle data in divergent-beam ct*, Journal of X-Ray Science and Technology, 14 (2006), pp. 119−139, 2006.

[28] E.Y. Sidky and X. Pan, *Image reconstruction in circular cone-beam computed tomography by constrained, total-variation minimization*, Phys. Med. Biol. 53 (2008), p. 4777.

[29] G.T. Herman and R. Davidi, *Image reconstruction from a small number of projections*, Inverse Probl. 24 (2008), p. 045011.

[30] J. Tang, B.E. Nett, and G.-H. Chen, *Performance comparison between total variation (TV)-based compressed sensing and statistical iterative reconstruction algorithms*, Phys. Med. Biol. 54 (2009), p. 5781.

[31] X. Duan, L. Zhang, Y. Xing, Z. Chen, and J. Cheng, *Few-view projection reconstruction with an iterative reconstruction-reprojection algorithm and TV constraint*, IEEE Trans. Nuclear Sci. 56 (2009), pp. 1377–1382.

[32] J. Bian, J.H. Siewerdsen, X. Han, E.Y. Sidky, J.L. Prince, C.A. Pelizzari, and X. Pan, *Evaluation of sparse-view reconstruction from flat-panel-detector cone-beam CT*, Phys. Med. Biol. 55 (2010), p. 6575.

[33] J. Bian, X. Han, E.Y. Sidky, G. Cao, J. Lu, O. Zhou, and X. Pan, *Investigation of sparse data mouse imaging using micro-CT with a carbon-nanotube-based X-ray source*, Tsinghua Sci. Technol. 15 (2010), pp. 74–78.

[34] X. Jia, Y. Lou, R. Li, W.Y. Song, and S.B. Jiang, *GPU-based fast cone beam CT reconstruction from undersampled and noisy projection data via total variation*, Med. Phys. 37 (2010), pp. 1757–1760.

[35] T.L. Jensen, J.H. Jørgensen, P.C. Hansen, and S.H. Jensen, *Implementation of an optimal first-order method for strongly convex total variation regularization*, BIT Numer Math. 52 (2012), pp. 329–356.

[36] Z. Tian, X. Jia, K. Yuan, T. Pan, and S.B. Jiang, *Low-dose CT reconstruction via edge-preserving total variation regularization*, Phys. Med. Biol. 56 (2011), p. 5949.

[37] A. Mohammad-Djafari and C. Soussen, *Reconstruction of Compact Homogeneous 3D Objects from their Projections*, in *Discrete Tomography — Foundations, Algorithms and Applications*, G. T. Herman and A. Kuba, eds., Birkäuser, Boston, 1999, pp. 317–342.

[38] C. Soussen and A. Mohammad-Djafari, *Polygonal and polyhedral contour reconstruction in computed tomography*, IEEE Trans. Image Process. 13 (2004), pp. 1507–1523.

[39] M. Allain and J. Idier, *Efficient binary reconstruction for non-destructive evaluation using gammagraphy*, Inverse Probl. 23 (2007), p. 1371.

[40] M. Robini, A. Lachal, and I. Magnin, *A stochastic continuation approach to piecewise constant reconstruction*, IEEE Trans. Image Process. 16 (2007), pp. 2576–2589.

[41] V. Singh, L. Mukherjee, P.M. Dinu, J. Xu, and K.R. Hoffmann, *Limited view CT reconstruction and segmentation via constrained metric labeling*, Comput. Vision Image Understanding 112(1) (2008), pp. 67–80.

[42] Y. Ting Lin, A. Ortega, and A. Dimakis, *Sparse recovery for discrete tomography*, 17th IEEE International Conference on Image Processing (ICIP), Hong Kong, September 2010, pp. 4181–4184.

[43] D.F. Yu and J.A. Fessler, *Edge-preserving tomographic reconstruction with nonlocal regularization*, IEEE Trans. Med. Imag. 21 (2002), pp. 159–173.

[44] H. Feng, W. Karl, and D. Castanon, *A curve evolution approach to object-based tomographic reconstruction*, IEEE Trans. Image Process. 12 (2003), pp. 44–57.
[45] R. Ramlau and W. Ring, *A Mumford–Shah level-set approach for the inversion and segmentation of X-ray tomography data*, J. Comput. Phys. 221 (2007), pp. 539–557.
[46] V. Kolehmainen, M. Lassas, and S. Siltanen, *Limited data X-ray tomography using nonlinear evolution equations*, SIAM J. Sci. Comput. 30 (2008), pp. 1413–1429.
[47] S. Yoon, A.R. Pineda, and R. Fahrig, *Simultaneous segmentation and reconstruction: A level set method approach for limited view computed tomography*, Med. Phys. 37 (2010), pp. 2329–2340.
[48] E. Klann, R. Ramlau, and W. Ring, *A Mumford-Shah level-set approach for the inversion and segmentation of SPECT/CT data*, Inverse Probl. Imag. 5 (2011), pp. 137–166.
[49] C. Popa and R. Zdunek, *Kaczmarz extended algorithm for tomographic image reconstruction from limited-data*, Math. Comput. Simul. 65 (2004), pp. 579–598.
[50] H.Y. Liao, *A gradually unmasking method for limited data tomography*, Biomedical Imaging: 4th IEEE International Symposium on Nano to Macro, Washington, DC, April 2007, pp. 820–823.
[51] K. Hanson, G. Cunningham, J. Jennings, G.R., and D. Wolf, *Tomographic reconstruction based on flexible geometric models*, IEEE International Conference on Image Processing, Vol. 2, Austin, TX, November 1994, pp. 145–147.
[52] X.L. Battle, G.S. Cunningham, and K.M. Hanson, 3*D tomographic reconstruction using geometrical models*, in *Society of Photo-Optical Instrumentation Engineers (SPIE) Conference Series*, K.M. Hanson, ed., Vol. 3034, San Jose, CA, February 1997, pp. 346–357.
[53] K.M. Hanson, G.S. Cunningham, and R.J. McKee, *Uncertainties in tomographic reconstructions based on deformable models*, in *Medical Imaging: Image Processing, Proceedings of SPIE*, K.M. Hanson, ed., Newport Beach, CA, February 1997, pp. 276–286.
[54] X.L. Battle, K.M. Hanson, and G.S. Cunningham, *Tomographic reconstruction using 3D deformable models*, Phys. Med. Biol. 43 (1998), pp. 983–990.
[55] A. Mohammad-Djafari and K. Sauer, *Shape reconstruction in X-ray tomography from a small number of projections using deformable models*, 17th International Workshop on Maximum Entropy and Bayesian Methods (MaxEnt97), Boise, ID, August 1997.
[56] J. Kybic, T. Blu, and M.A. Unser, *Variational approach to tomographic reconstruction*, in *Society of Photo-Optical Instrumentation Engineers (SPIE) Conference Series*, M. Sonka and K. M. Hanson, ed., Vol. 4322, San Diego, CA, July 2001, pp. 30–39.
[57] S. Do, W. Karl, M. Kalra, T. Brady, and H. Pien, *A variational approach for reconstructing low dose images in clinical helical CT*, Biomedical Imaging: IEEE International Symposium on Nano to Macro, Rotterdam, The Netherlands, April 2010, pp. 784–787.
[58] E.J. Candès, J. Romberg, and T. Tao, *Robust uncertainty principles: exact signal reconstruction from highly incomplete frequency information*, IEEE Trans. Inform. Theory 52 (2006), pp. 489–509.
[59] D. Calvetti and E. Somersalo, *Microlocal sequential regularization in imaging*, Inverse Probl. Imag. 1 (2007), pp. 1–11.
[60] H. Yu and G. Wang, *Compressed sensing based interior tomography*, Phys. Med. Biol. 54 (2009), p. 2791.
[61] H. Yu and G. Wang, *A soft-threshold filtering approach for reconstruction from a limited number of projections*, Phys. Med. Biol. 55 (2010), p. 3905.
[62] K. Choi, J. Wang, L. Zhu, T.-S. Suh, S. Boyd, and L. Xing, *Compressed sensing based cone-beam computed tomography reconstruction with a first-order method*, Med. Phys. 37 (2010), pp. 5113–5125.
[63] X. Jia, B. Dong, Y. Lou, and S.B. Jiang, *GPU-based iterative cone-beam CT reconstruction using tight frame regularization*, Phys. Med. Biol. 56 (2011), p. 3787.
[64] H. Langet, C. Riddell, Y. Trousset, A. Tenenhaus, E. Lahalle, G. Fleury, and N. Paragios, *Compressed sensing based 3D tomographic reconstruction for rotational angiography*, in *Medical Image Computing and Computer-Assisted Intervention MICCAI 2011*, G. Fichtinger, A. Martel,

and T. Peters, eds., Vol. 6891, Lecture Notes in Computer Science, Springer, Berlin, Heidelberg, 2011, pp. 97–104.

[65] S. Siltanen, V. Kolehmainen, S. Järvenpää, J.P. Kaipio, P. Koistinen, M. Lassas, J. Pirttilä, and E. Somersalo, *Statistical inversion for X-ray tomography with few radiographs I: General theory*, Phys. Med. Biol. 48 (2003), pp. 1437–1463.

[66] J. Kaipio and E. Somersalo, *Statistical and Computational Inverse Problems*, Applied Mathematical Sciences, Vol. 160, Springer-Verlag, New York, 2005.

[67] D. Calvetti and E. Somersalo, *Priorconditioners for linear systems*, Inverse Probl. 21 (2005), pp. 1397–1418.

[68] M. Rantala, S. Vänskä, S. Järvenpää, M. Kalke, M. Lassas, J. Moberg, and S. Siltanen, *Wavelet-based reconstruction for limited-angle X-ray tomography*, IEEE Trans. Med. Imag. 25 (2006), pp. 210–217.

[69] K. Niinimäki, S. Siltanen, and V. Kolehmainen, *Bayesian multiresolution method for local tomography in dental X-ray imaging*, Phys. Med. Biol. 52 (2007), pp. 6663–6678.

[70] C. Soussen and J. Idier, *Reconstruction of three-dimensional localized objects from limited angle X-ray projections: an approach based on sparsity and multigrid image representation*, J. Electr. Imag. 17 (2008), p. 033011.

[71] S. Vänskä, M. Lassas, and S. Siltanen, *Statistical X-ray tomography using empirical Besov priors*, Int. J. Tomogr. Stat. 11 (2009), pp. 3–32.

[72] E. Klann, R. Ramlau, and L. Reichel, *Wavelet-based multilevel methods for linear ill-posed problems*, BIT 51 (2011), pp. 669–694.

[73] G.T. Herman and A. Kuba, *Discrete Tomography: Foundations, Algorithms, and Applications*., Birkäuser, Boston, 1999.

[74] G.T. Herman and A. Kuba, *Advances in Discrete Tomography and its Applications*, Applied and Numerical Harmonic Analysis, Birkhäuser Boston, Boston, MA, 2007.

[75] Julianne Chung, Glenn Easley, and Dianne P. O'Leary, *Windowed Spectral Regularization of Inverse Problems*, SIAM J. Sci. Comput. 33(6) (2011), pp. 3175–3200.

[76] N. Wiener, *Extrapolation, Interpolation and Smoothing the Stationary Time Series*, The MIT Press, Cambridge, MA, 1942.

[77] H.C. Andrews and B.R. Hunt, *Digital Image Restoration*, Prentice Hall, New Jerry, 1977.

[78] S.E. Umbaugh, *Computer Imaging: Digital Image Analysis and Processing*, CRC Press, Boca Raton, 2005.

[79] B.R. Hunt, *The application of constrained least squares estimation to image restoration by digital computer*, IEEE Trans Comput. C-22(9) (1973), pp. 805–812.

[80] H.E. Lu and A. Antoniou, *Two-dimensional Digital Filters*, Marcel Dekker, New York, 1992.

[81] R.C. Gonzalez and R.E. Woods, *Digital Image Processing*, 3rd ed., Pearson Education, Upper Saddle River, NJ, 2008.

[82] E.S. Ribeiro, N. Mascarenhas, F. Salina, and P. Cruvinel, *Noise reduction on CT Set of projections by wiener filtering and wavelet thresholding*, VI Workshop de Visão Computacional, Sao Paolo, Brazil, July 2010.

[83] M. Tabuchi, N. Yamane, and Y. Morikawa, *Adaptive Wiener filter based on gaussian mixture model for denoising chest X-ray CT image*, SICE Annual Conference, Takamatsu City, Japan, September 2007.

[84] M. Hussien, M. Saripan, *Computed tomography soft tissue restoration using Wiener filter* Proceedings of 2010 IEEE Student Conference on Research and Development, Putrayaja, Malaysia, December 2010.

[85] F. Yoshinori, N. Yoshio, and M. Shimamura, *Reduction of artifacts in degraded CT image by adaptive Wiener filter*, Jpn. J. Med. Electron. Biol. Eng. 40(1) (2002), pp. 1–6.

[86] W. Shao, J. Ni, and C. Zhu, A hybrid method of image restoration and denoise of CT images Sixth International Conference on Internet Computing for Science and Engineering (ICICSE), Zhengzhou, China, April 2012.

[87] L. Ke, R. Zhang, *Multiscale wiener filtering method for low-dose CT Images*, 3rd International Conference on Biomedical Engineering and Informatics, Yantai, China, October 2010.

[88] L. Wang, G. Chen, N. Lu, and N. Jiang, *A medical CT image enhancing algorithm based on the mixture scope model of wavelet multi-scale transform*, Second International Symposium on Intelligent Information Technology Application, 2008.

[89] E.Y. Sidky, C.M. Kao, and X. Pan. Effect of the data constraint on few-view, fan-beam CT image reconstruction by TV minimization, *Nuclear Science Symposium Conference Record*, IEEE, Philadelphia, Vol. 4, 2006, pp. 2296–2298.

[90] Epstein C, Introduction to the Mathematics of Medical Imaging (2nd Edition), SIAM 2008.

[91] L. Elden, L. Wittmeyer-Koch, and H. Nielsen, *Introduction to Numerical Computation*, Sudetliteratur, Lund, 2004.

[92] H. Kostler, M. Prummer, U. Rude, and J. Hornegger, *Adaptive variational sinogram interpolation of sparsely sampled CT data*, 18th International Conference on Pattern Recognition, 2006. ICPR 2006. Vol. 3, Hong Kong, August 2006, pp. 778–781.

[93] M. Bertram, G. Rose, D. Schafer, J. Wiegert, and T. Aach, *Directional interpolation of sparsely sampled cone-beam CT sinogram data*, Biomedical Imaging: IEEE International Symposium on Nano to Macro, Arlington, VA, 15–18 April 2004, Vol. 1, pp. 928–931.

[94] A. Dhawan, R.M. Rangayyan, and R. Gordon, *Image restoration by Wiener deconvolution in limited-view computed tomography*, Appl. Optics 24(23) (1985), pp. 4013–2020.

[95] J.S. Jaffe, *Limited angle reconstruction using stabilized algorithms*, IEEE Trans. Med. Imag. 9(3) (1990), pp. 338–244.

[96] R. Zdunek, Z. He, and A. Cichocki, *Tomographic image reconstruction from limited-view projections with Wiener filtered FOCUSS algorithm*, 5th IEEE International Symposium on Biomedical Imaging: From Nano to Macro, Paris, France, April 2008, pp. 768–771.

[97] I.F. Gorodnitsky and B.D. Rao, *Sparse signal reconstruction from limited data using FOCUSS: A re-weighted minimum norm algorithm*, IEEE Trans. Signal Process. 45(3) (1997), pp. 600–615.

[98] A. Ozcan, A. Bilenca, A. Desjardins, B. Bouma, and G. Tearney, *Speckle reduction in optical coherence tomography images using digital filtering*, J. Optical Soc. Am. 24(7) (2007), pp. 1901–1910.

[99] A. Pralat and R. Zdudek, *Regularized image reconstruction in the electromagnetic geotomography through the use of the Wiener filter*, International Conference on Mathematical Methods in Electromagnetic Theory, Kharkov, Ukraine, September 2000, pp. 607–609.